A combined Thomson-Rayleigh scattering diagnostic using an intensified photodiode array

A combined Thomson–Rayleigh scattering diagnostic using an intensified photodiode array

M. C. M. van de Sanden, G. M. Janssen, J. M. de Regt, D. C. Schram, J. A. M. van der Mullen, and B. van der Sijde
Department of Physics, Eindhoven University of Technology, P. O. Box 513, 5600 MB Eindhoven, The Netherlands

(Received 14 November 1991; accepted for publication 10 February 1992)

A combined Thomson–Rayleigh scattering device is discussed. It consists of a Nd:YAG laser as a light source in combination with a multichannel detection technique consisting of a gated light amplifier in combination with an optical multichannel analyzer. Special attention is focused on the analysis of the measured spectra. Including convolution methods and taking into account weak coherent effects increases the dynamic range and the accuracy of the measured electron density n_e and temperature T_e and neutral particle density n_0. Accuracies of 1%–4% for n_e, 2%–6% for T_e, and 10%–50% for n_0 depending on the plasma condition are obtained. The dynamic range for n_e is 7×10^{17}–10^{21} m^{-3}, for n_0 is 10^{20}–10^{23} m^{-3} and for T_e is 1000–50 000 K.

I. INTRODUCTION

Expanding plasmas have been a subject of extensive studies during the past decades.[1–5] The flow problem is usually characterized by a supersonic expansion which ends in the formation of a stationary normal shock front. After the shock front the plasma expands further subsonically. Studying expanding plasmas appropriate diagnostics to measure the densities and temperatures locally is essential. A good spatial resolution and a high accuracy with a large dynamic range are necessary since the gradients are large especially in the first supersonic region. Main parameters in expanding plasmas are the electron and neutral particle density and the electron temperature. Several diagnostics have been used to determine these parameters.

Langmuir probe measurements[1–4] yield consistent results for the electron density and temperature. The limit on this measurement is that the plasma is influenced by the probe itself and the precision in T_e is limited. Furthermore, the presence of negative ions is a complication.[3] Measuring the Stark width of (hydrogen) spectral lines gives also good results for the electron density[5] for higher electron densities. A severe problem here is the necessity of Abel inversion on every wavelength position to get local information. Besides this, other broadening mechanisms can blur the Stark broadening totally. Other possibilities are line intensities[2–7] in combination with or without continuum measurements.[8] Both have as a disadvantage that an Abel inversion has to be performed and in case of neutral particle density[2] or electron temperature determination[6,7] model assumptions have to be made. These model assumptions can cause large uncertainties in the determined parameters. A method to determine the plasma density is interferometry.[7–10] Usually this diagnostic is combined with another diagnostic to determine either the electron or the neutral particle density. Also in this case local information is only obtained after Abel inversion. Another possibility to gain information of the plasma is to measure the pressure with a Pitot tube.[6,11] The Pitot tube has the same disadvantage as the Langmuir probe, i.e., the Pitot tube changes the plasma. If one is only interested in qualitative information, Schlieren and shadow photography are also possible, if the plasma does not emit to much light by itself. The last two diagnostics are mainly used in flow studies to visualize the shock front occurring in, e.g., nozzle flows.

A method to determine the electron density and temperature in an expanding plasma is Thomson scattering.[7,8,10,12] The advantages over the diagnostics mentioned above is the fact that it measures the electron density and temperature locally and no model assumptions are necessary. Unfortunately Thomson scattering is very weak and only when powerful lasers came available Thomson scattering became popular.[13] A method related to Thomson scattering is Rayleigh scattering. It is used to determine the neutral particle density locally.[14,15] A key problem here is the stray light because one cannot distinguish it from the Rayleigh scattering signal. Combining the two scattering diagnostics is very convenient in studying expanding plasmas because the three important plasma parameters can be measured in one time. Only recently diagnostics which combine the two scattering techniques were developed.[16,17]

In this paper a new constructed combined Thomson and Rayleigh scattering setup is presented. As already mentioned a key problem in developing a Thomson–Rayleigh scattering setup is the level of the stray light. The level in the new setup is diminished to 0.4-Pa argon at 295 K making possible the measurement of neutral particle densities down to 10^{20} m^{-3}. The diagnostic is used to measure n_e, n_0, and T_e in an expanding magnetized cascaded arc plasma, which, depending on the operating mode, has electron densities in the range 5×10^{17}–10^{21} m^{-3}, neutral particle densities in the range 10^{20}–10^{23} m^{-3}, and electron temperatures of 1000–25 000 K. This large dynamic range is achieved by using a powerful periodically pulsed Nd:YAG laser in combination with a multichannel detection consisting of a gated light amplifier and an optical multichannel analyzer (OMA). The OMA is

 0034-6748/92/063369-09$02.00

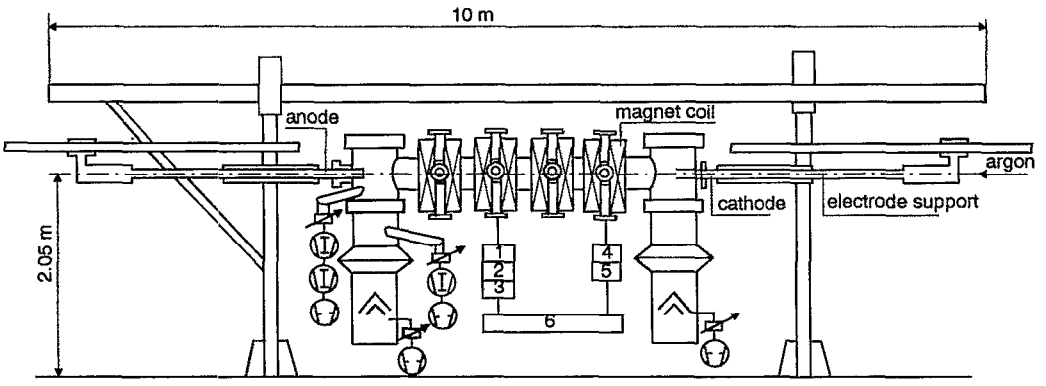

FIG. 1. The cascaded arc setup.

cooled which permits long integration times. So in contrast to some tokamak Thomson scattering systems[18] which accumulate individual laser shots in a computer, in our system the scattered signal is integrated as the signal-to-noise ratio improves until sufficient precision is reached. The large dynamic range in T_e for our system is achieved by a high-resolution grating and by using convolution techniques. Convolution techniques can be used since the apparatus profile is known from the calibration measurements. Because an OMA is used it is possible to measure the total Thomson–Rayleigh spectrum. Therefore deviations from a Maxwellian distribution function can be studied easily. A high resolution can also be achieved by scanning a dye laser and detection in a small bandwidth. In Ref. 9 an experiment is in which one was able to resolve the ion feature for a scattering parameter in the range 1–2.

The outline of the paper is as follows. In Sec. II, the plasma device is discussed. This section will be followed by a description of the Thomson–Rayleigh setup, the calibration procedure, and the way in which the measurements are analyzed. In Sec. IV the results are presented.

II. DESCRIPTION OF THE MAGNETIZED EXPANDING CASCADED ARC

Figure 1 shows the general outline of the plasma setup. It consists of a cascaded arc as a plasma source and an auxiliary end anode positioned in a stainless-steel vessel. The vessel is pumped to low pressure by means of two diffusion pumps or a large roots pump (2600 m^3/h) and is surrounded by eight Helmholtz coils which can apply a magnetic field in the range from 0 to 0.5 T. The cascaded arc (Fig. 2), introduced by Maecker[20] consists of three (tungsten-thorium) cathodes at one end, a stack of eight water cooled copper plates insulated electrically from each other by PVC spacers and vacuum sealed by O rings, and an anode plate at the other end. Through the copper cascade plates and the anode plate there is a 4-mm bore forming a central channel of approximately 50-mm length. The discharge is created between the cathodes and the anode plate. The plasma created is a flowing subatmospheric thermal plasma (flow 8–100 scc/s) with currents in the range of 30–100 A. The electron density is in the range of 10^{21}–10^{24} m^{-3} and the electron and heavy particle temperatures are in the 10^4-K range. At the exit the plasma expands into the vessel at low pressure (1–100 Pa). Argon is used as a carrier gas. Beside the current in the cascaded arc, current can also be drawn in the jet section by applying a voltage between the cathodes and the auxiliary end anode. In this mode the plasma jet has similar characteristics as the hollow cathode arc[21] depending on background pressure. A main difference and advantage compared with the hollow cathode arc is the presence of the cascaded arc which has a much longer lifetime than the hollow cathode.

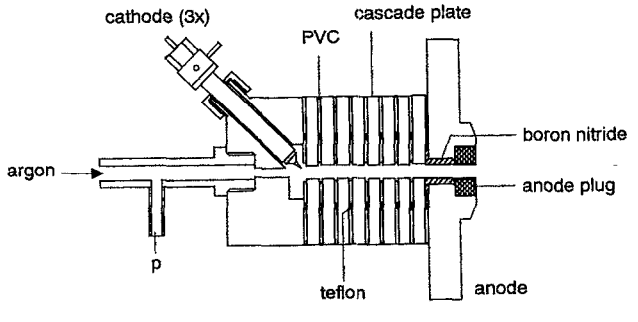

FIG. 2. The cascaded arc.

A similar setup as shown in Fig. 1 was used by Kroesen *et al.*[22] and Beulens *et al.*[23] to deposit hydrogenated carbon layers and by Meeusen *et al.*[24] to make hydrogenated silicon layers, where methane or silane are injected in the plasma jet. An important difference is the presence of a magnetic field.

The expanding magnetized cascaded arc is mainly used for transport studies. For this purpose several diagnostics are present: Fabry–Pérot interferometry for measuring neutral particle and ion temperatures and axial and azimuthal neutral particle and ion velocities. Optical spectroscopy for determining the plasma equilibrium and the Thomson–Rayleigh scattering setup for measuring the electron and neutral particle density and the electron temperature. The Thomson–Rayleigh scattering will be discussed more extensively in the next sections.

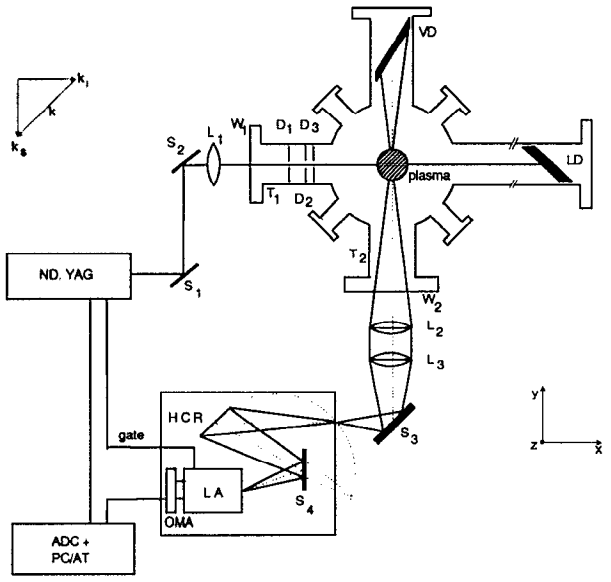

FIG. 3. The Thomson–Rayleigh scattering setup. Note that the polychromator is viewed from the top.

III. THE THOMSON–RAYLEIGH SCATTERING DIAGNOSTIC

A. Description of the setup

In Fig. 3 the Thomson–Rayleigh scattering setup is depicted. The scattering plane is normal to the jet axis. A frequency-doubled Nd:YAG laser (DCR 11 Quanta Ray, $E_{\text{pulse}} = 0.19$ J/shot, $\tau_{\text{pulse}} = 10$ ns, $f_{\text{ep}} = 10$ Hz) at $\lambda_0 = 532$ nm is used. Two dichroic mirrors are necessary to select the green light which is focused into the plasma by the lens $L_1 (f = 500$ mm) to a waist of 0.5 mm ($1/e$ width). The infrared photons are absorbed by the beam dumps behind S_1 and S_2. To diminish the stray light due to scattering on the entrance window several diaphragms are installed in the vessel tube T_1. The lens L_1 and the window W_1 are antireflection coated for a wavelength band around $\lambda_0 = 532$ nm. The length of the exit tube is chosen as large as possible to diminish the solid angle under which the reflected light of the laser dump can enter the vessel again and cause unwanted stray light. The incident laser light is absorbed in the laser dump, which is mounted on the large tube. The laser dump consists of a glass plate NG3 under the Brewster angle. The 90° scattered light is observed through the window W_2. The scattered light is then imaged on the entrance slit of the polychromator by two plano convex lenses L_2 and L_3 (both $f = 500$ mm). Matching the aperture ratio of the detection optics to the aperture ratio of the holographic grating (special Jobin Yvon; 1800 ℓ/mm; Rowland geometry; dispersion of Rowland circle 1.11 nm/mm) leads to a solid angle of 2.5×10^{-2} sr. The entrance and exit angle of the polychromator are chosen in such way that the main aberrations are minimal on the Rowland circle for the wavelength $\lambda_0 = 532$ mm.[25] The scattered light is detected against a black background by means of a viewing dump which consists of a glass plate under the Brewster angle. To reduce the stray light further a set of diaphragms are mounted in the viewing tube T_2 which are matched to the solid angle.

The mentioned precautions as laser dump, large exit tube, viewing dump, antireflection coatings, diaphragms etc. diminish the stray light to a level of 0.4-Pa argon at 295 K. This corresponds to an electron density of 5×10^{17} m^{-3} and a neutral particle density of 7×10^{19} m^{-3}. This level is two orders of magnitude larger than obtained by Jauernik *et al.*,[16] but is two orders of magnitude lower than obtained by Marshall and Hieftje.[26] The reason for the large difference in the level of stray light between the present setup and the setup of Jauernik *et al.*[16] is the difference in solid angle $\Delta\Omega$, i.e., the stray light comes from reflections of the total vessel whereas the scattered signal originates from a well defined solid angle. The level of 7×10^{19} m^{-3} with an accuracy of the same order makes it possible to measure neutral particle densities larger than 10^{20} m^{-3} with an accuracy of 50%. Electron densities as low as 7×10^{17} m^{-3} are measurable with the same accuracy. Note that the accuracy in the determination of n_0 not only depends on the level of stray light but also on the electron temperature. The higher the electron temperature the higher the accuracy in n_0 because then the error due to the signal in the central Thomson channel is lower. Therefore, it can be concluded that the unwanted stray light is limited to a level which is low enough to enable neutral particle and electron density measurements in the expanding magnetized cascaded arc.

As already mentioned, the scattered light is dispersed by the holographic grating. Together with the width of the entrance slit (0.5 mm) and the dispersion of the grating this leads to a wavelength resolution of 0.36 nm if the slit is totally illuminated by the scattered light. Since the waist of the laser beam (FWHM) in the focus is 0.5 mm this condition is fulfilled. The resolution, however, is much improved by convolution methods as will be shown later. The height of the entrance slit gives the spatial resolution in the radial direction which is 1 mm. The beam diameter and the dimensions of the entrance slit determine the detection volume of 0.25 mm^3.

The detector of the Thomson–Rayleigh scattering consists of three parts: a gated light amplifier (LA), an optical multichannel analyzer (OMA), and a personal computer with an ADC plug in unit (12 bits, 100-kHz DMA). The gated light amplifier (proximity focused containing a microchannel plate, amplification 10000×, $\tau_{\text{gate}} = 20$ ns, straight fiber optic) amplifies the light which strikes the photocathode (S20, quantum efficiency 12% at 532 nm). The photocathode is positioned on the Rowland circle. At the exit of the light amplifier the emitted green light is, by means of camera optics, focused onto an optical multichannel analyzer (1024 pixels; 25-μm × 2.5 mm EG&G Reticon photo diode array RL1024S). The light amplifier is gated by an advanced trigger pulse provided by the Nd:YAG laser. This advanced signal triggers the high voltage pulse of the light amplifier (on/off ratio $> 10^6$). The OMA is cooled by means of two peltier elements ($T_{\text{OMA}} = -20$ °C) which provides long integration times (over 4 min). After a certain amount of laser shots the accumulated Thomson–Rayleigh spectrum contained in

the OMA is scanned and the analog signal is converted to a digital signal by the ADC plug in unit in the personal computer. The light amplifier together with the OMA acts as a "nearly" photon counter. The relation can be calculated theoretically and is given by[27]

$$1 \text{ ADC count} \simeq 3.4 \text{ photoelectrons.} \quad (1)$$

Neglecting the possible noise sources which will be discussed further on, it follows from Eq. (1) that if a 14-bit AD converter would be used, single-photon counting can be performed. This is in principle possible since the dynamic range of the photodiode array is approximately 10^4.

The described detector has several advantages compared to other described detectors.[16,26] First it has one gating element. This is a large advantage compared to an array of gated photomultipliers since the timing is much easier. Second because the photocathode of the light amplifier has a width of 17 mm, corresponding to a wavelength scale of approximately 19 nm, the total spectrum can be measured in one time in channels of a width of approximately 28 pm. In this way it is possible to measure deviations from a Maxwell distribution due to for example electron runaway or a current density.[28] The third advantage, related to the second, is the fact that during Rayleigh calibration the apparatus profile is measured which can be used in the analysis of the measured spectra. This leads to higher accuracy compared to other setups where the apparatus profile is assumed[16] or where no correction is performed for the apparatus profile.[17,26,29] Fourth, as we shall see later, since the OMA integrates the signal the calibration can be performed under the same conditions as the Thomson–Rayleigh spectra. In this way there is no problem concerning the different time response of the detector elements since dc calibration measurements can be omitted.

Compared to the detectors consisting of one photomultiplier[19,30] the described detector has the advantage that no wavelength scan has to be made. In contrast to other similar setups the incident laser light intensity is not measured simultaneously.[16,26] This has two reasons. The first one is the fact that the inhomogeneous distribution of the laser energy in the laser beam makes it uncertain that the laser energy measured somewhere in the setup is a measure for the energy actually in the scattering volume. Second during laser stability tests the laser energy is stable within 2% during more than 6 h. Care is taken that the measuring time does not extend this 6 h of operation. Since all the measurements are averaged over 1200 shots the variations in the energy distribution in the laser beam can be neglected, in fact they are measured during the calibration measurements (see next section).

The measurements of the Thomson–Rayleigh profiles in radial and axial direction are performed by moving electrode supports (Fig. 1). The advantage is that the optics remain fixed. Differences due to a nonhomogeneous magnetic field (if applied) both in axial and in radial direction of the plasma parameters are assumed to lie within the experimental errors.

TABLE I. Characteristics.

Laser energy	E_{pulse}	0.19	J/pulse
Number of shots	N_{shot}	1200	
Scattering angle	θ	$\pi/2$	
Solid angle	$\Delta\Omega$	2.5×10^{-2}	sr
Length of det. volume	L_{det}	1.0	mm
Detection volume	V_{det}	0.25	mm^3
Stray light level		0.4	Pa argon
in n_0		7×10^{19}	m^{-3}
in n_e		5×10^{17}	m^{-3}
Detection limit			
in n_0		10^{20}	m^{-3}
in n_e		7×10^{17}	m^{-3}
electrons in detection volume		1.8×10^{8}	
Dynamic range			
in n_0		10^{20}–10^{23}	m^{-3}
in n_e		$5\ 10^{17}$–10^{21}	m^{-3}
in T_e		1000–50 000	K

To summarize: the main characteristics of the setup are a high repetition, short pulse Nd:YAG laser as a light source and multichannel detection consisting of a polychromator, a gated light amplifier, and an OMA system. The amplifier takes care of the amplification and gating of the individual shots of the laser signal while the OMA integrates the total signal for a number of laser shots. The main parameters of the setup are listed in Table I. The low detection limit for n_e and n_0 is a consequence of low vessel stray light level and is equal to 10^{20} m^{-3} for n_0 and 7×10^{17} m^{-3} for n_e. The lower limit for T_e is determined by the width of the apparatus profile while the upper limit is a consequence of the size of the detector surface. As can be seen from Table I the dynamic range for all three parameters is large.

B. Calibration and analysis

To deduce absolute results from the Thomson–Rayleigh spectra the setup needs to be calibrated relatively and absolutely and the dispersion of the polychromator has to be obtained. Furthermore, the measured profiles have to be corrected for the plasma light and the stray light. It appeared that the plasma light correction is only necessary for the high electron temperatures ($T_e > 1$ eV). In that case the plasma light is measured under identical measurement and plasma conditions, however, without laser light being present. The stray light is measured by pumping the vessel to low pressure ($< 10^{-2}$ Pa). For measurements at positions close to the exit of the cascaded arc (< 12 mm) the stray light was measured directly after every measurement. This is necessary because putting the cascaded arc back at the exactly same position is practically impossible and would otherwise lead to an increase of the inaccuracy. The relative calibration of the pixels and the light amplifier is done under the same conditions as the plasma measurements using a tungsten ribbon lamp. This is possible since the OMA integrates the signal. This is an advantage of the use of the gated light amplifier compared to the use of an array of photomultipliers. Usually dc measurements of the relative calibration are done[16] leaving an uncertainty in the time response of the different photomultipliers. In the

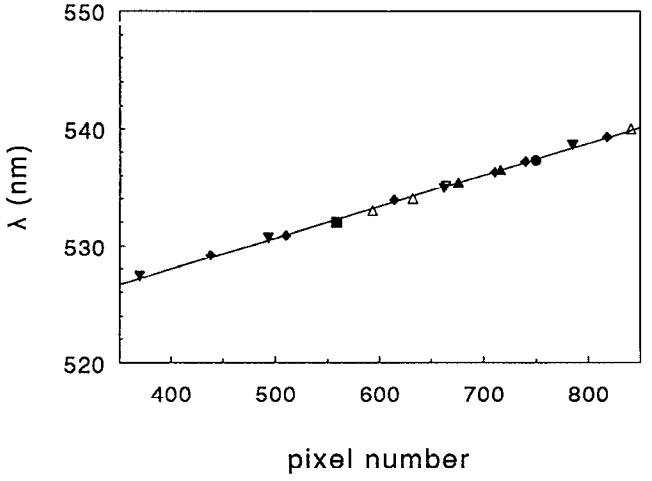

FIG. 4. The wavelength of several emission lines of different gas discharge lamps as a function of the pixel number (△) Ne, (▼) Cs, (♦) Xe, (▲) Hg, (●) Ar, (▽) Ti, and (■) Nd:YAG.

other case a fast pulsed light emitting diode (LED) is used[26] having the uncertainty of the wavelength dependent emission of the LED. The calibration of the wavelength scale, i.e., the measurement of the dispersion on the Rowland circle is done by using gas discharge lamps with well defined spectral lines in the area around $\lambda_0 = 532$ mm. The light amplifier is not in the gated mode during these measurements, but is set in the continuous mode. The measurement is only done for determining the dispersion, i.e., no absolute wavelength scale is obtained. The effect of the Rowland circle in combination with a flat detection surface is also studied since this influences the linear relation between position of the spectral lines and the pixel number. In Fig. 4 the calibration of the wavelength scale is given. As can be seen a straight line is found with good correlation (0.9991).

The absolute calibration is performed using an argon gas sample (typically 200 Pa) and performing a measurement under the same conditions as during the plasma measurements. Knowing the ratio between the Rayleigh for $\lambda_0 = 532$ mm and the Thomson cross section and measuring the pressure and the temperature of the gas sample, a relation can be determined between the density and the amount of ADC counts. The absolute calibration is repeated every 1 or 2 h to obtain the highest accuracy in the determination of n_e and n_0. During the measurements the variation in the calibration factors is within 2% and are due to the variation of the laser energy and energy distribution within the laser beam. Since the relative calibration does not depend on the laser, this calibration is performed less frequently than the absolute calibration.

The absolute calibration is also used for another purpose. Because of the width of the entrance slit, the profile measured during the absolute calibration is equal to a convolution of the apparatus profile of the polychromator and detector, the line profile of the laser and the spectrum due to the random motion of the argon atoms in the gas sample. A quick estimate of the $1/e$ width of the apparatus profile (≈ 16 pixels) shows that it is much broader than

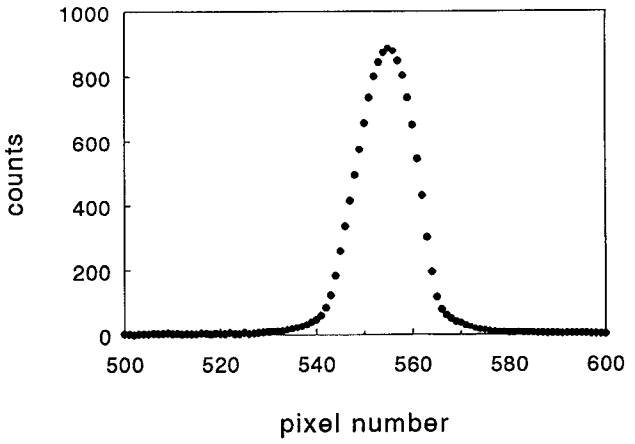

FIG. 5. The measured apparatus profile.

the width of the line profile of the laser (< 1 pixel) and the width due to the temperature motion of the argon gas atoms (< 1 pixel). Thus the profile measured during the absolute calibration is in the apparatus profile. An example is shown in Fig. 5. As can be seen the apparatus profile is not symmetric which has consequences for the Thomson–Rayleigh measurements if the measured electron temperatures are low. The asymmetric apparatus profile is probably due to imperfect slits, inhomogeneous energy distribution of the laser beam etc. As already mentioned the knowledge of the apparatus profile is an advantage of our setup compared to the other setups which use an array of photomultipliers. In Table II the differences are indicated if instead of the asymmetric apparatus profile a Gaussian is taken with the same width.[16] The weighted least mean square analysis was performed on a simulated Thomson–Rayleigh spectrum using the measured apparatus profile. As can be seen the influence on T_e is significant especially if T_e is low. The influence on n_0 is related to the

TABLE II. Influence of the asymmetric apparatus profile.

	Method I			Method II		
	$\frac{\Delta n_2}{n_e}$	$\frac{\Delta T_e}{T_e}$	$\frac{\Delta n_0}{n_0}$	$\frac{\Delta n_e}{n_e}$	$\frac{\Delta T_e}{T_e}$	$\frac{\Delta n_0}{n_0}$
1	0.005	0.022	0.001	0.084	0.085	0.074
2	0.089	0.15	0.063	0.14	0.052	0.063
3	0.002	0.02	0.008	0.002	0.11	0.022
4	0.004	0.004	0.000	0.002	0.019	0.062
5	0.001	0.008	0.055	0.41	0.33	···
6	0.000	0.003	0.006	0.001	0.034	0.046

Method I: The analysis is performed by using the measured apparatus profile.

Method II: The analysis is performed by using a Gaussian apparatus profile with the same $1/e$ width as the measured apparatus profile.

1: $n_e = 5\times10^{18}$ m^{-3}, $n_0 = 10^{21}$ m^{-3} and $T_e = 5800$ K
2: $n_e = 5\times10^{18}$ m^{-3}, $n_0 = 10^{21}$ m^{-3} and $T_e = 17400$ K
3: $n_e = 5\times10^{19}$ m^{-3}, $n_0 = 10^{21}$ m^{-3} and $T_e = 5800$ K
4: $n_e = 5\times10^{19}$ m^{-3}, $n_0 = 10^{21}$ m^{-3} and $T_e = 17400$ K
5: $n_e = 5\times10^{20}$ m^{-3}, $n_0 = 10^{21}$ m^{-3} and $T_e = 5800$ K
6: $n_e = 5\times10^{20}$ m^{-3}, $n_0 = 10^{21}$ m^{-3} and $T_e = 17400$ K

influence on T_e since T_e determines the width of the profile and thus the height of the Thomson component.

The analysis of the measured spectra is done as follows. The Thomson–Rayleigh profile $P(\omega-\omega_0)$ can be written as

$$P(\omega-\omega_0)d\omega = O_T S(\mathbf{k},\omega-\omega_0)d\omega + O_R\delta(\omega-\omega_0)d\omega. \quad (2)$$

Here O_T is proportional to the electron density n_e and O_R is proportional to the ground state neutral particle density n_0 and the ground state ion density n_i. The spectral density function $S(\mathbf{k},\omega-\omega_0)$ for a Maxwellian distribution function for the electrons to order α^2 is given by[31]

$$S(\mathbf{k},\omega-\omega_0) = (\pi^{1/2}kv_e)^{-1}\exp(-x_e^2) \times\{1-2\alpha^2\,\mathrm{Re}[w(x_e)]\}. \quad (3)$$

Here α is the scattering parameter given by $\alpha=(k\lambda_D)^{-1}$ with λ_D the Debye length [$\lambda_D=(\epsilon_0 k_b T_e/e^2 n_e)^{1/2}$], k is the amplitude of the scattering vector $\mathbf{k}$ [$k=2k_0\sin(\theta/2)$ with k_0 is the absolute value of the propagation vector $\mathbf{k}_0$ of the laser, θ is the angle between the incoming beam and the direction toward the observer], $v_e=(2k_bT_e/m_e)^{1/2}$ the thermal speed of the electrons in the scattering plane and $x_e=(\omega-\omega_0)/kv_e$. In Eq. (3) Re[$w(x_e)$] is the real part of the plasma dispersion function $w(x_e)$ given by[31]

$$w(x_e) = 1-2x_e\exp(-x_e^2)\int_0^{x_e}\exp(x^2)dx + i\sqrt{\pi}x_e\exp(-x_e^2). \quad (4)$$

For $\alpha \ll 1$ the Thomson profile is Gaussian and T_e can be determined from the $1/e$ width. Since the scattering plane is normal to the jet axis the Maxwellian velocity distribution is the distribution in radial sense. If $0<\alpha<0.5$, T_e and n_e are determined from the shape of the profile of $S(\mathbf{k},\omega-\omega_0)$ in combination with the surface O_T. The delta function in Eq. (2) is chosen to represent the Rayleigh component although the component has a finite width. However, as already indicated this width can be neglected compared to the width of the Thomson profile and the width of the apparatus profile. The measured profile $P^*(\omega-\omega_0)$ is a convolution of the apparatus profile $A(\omega_a)$ with the profile $P(\omega-\omega_0)$, i.e.,

$$P^*(\omega-\omega_0) = \int_{-\infty}^{\infty} A(\omega_a)P(\omega-\omega_0-\omega_a)d\omega_a. \quad (5)$$

In practice the profiles measured are analyzed using Eqs. (2), (3), and (5) in combination with a linear background in a seven parameter weighted least mean square analysis running on a personal computer. Note that is chosen for seven parameter weighted least mean square analysis. This is because the position of the Rayleigh component is chosen independent from the Thomson component since the apparatus profile is asymmetric. In this procedure the convolution is calculated using fast Fourier transforms. The weighted least mean squares analysis is based on the Levenberg–Marquardt iteration scheme.[32] A similar method was used by Huang and Hieftje,[17] although no convolution with the apparatus profile was performed.

TABLE III. Influence of coherent effects. The comparison was made for $n_e=1.7\times10^{20}$ m^{-3}, $n_0=3.6\times10^{21}$ m^{-3}, and $T_e=3400$ K corresponding to $\alpha=0.20$.

	Method III	Method IV
$\frac{\Delta n_e}{n_e}$	0.028	0.001
$\frac{\Delta T_e}{T_e}$	0.036	0.003
$\frac{\Delta n_0}{n_0}$	0.064	0.006

Method III: The analysis is performed not including coherent effects.
Method IV: The analysis is performed including coherent effects to order α^2.

From the parameter O_R the neutral particle density n_0 can be determined. Here the contribution of the ion ground state has to be subtracted. This contribution is equal to $0.393n_i$ (Ref. 16) relative to n_0 where $n_i=n_e$ because of quasineutrality. The influence of the excited states can be neglected since the densities are much lower than the ground state densities.[16,19] Using the explicit form of the apparatus profile increases the dynamic range of T_e (1000–50 000 K) and besides this, it takes into account the asymmetric apparatus profile properly which increases the accuracy.

To demonstrate the necessity of implementing coherent effects in the case of the expanding cascaded arc, a comparison was made (see Table III). Here the influence of taking into account coherent effects to order α^2 is depicted. A coherent profile was simulated using Eqs. (2), (3), and (5) with $n_e=1.7\times10^{20}$ m^{-3}, $T_e=3400$ K, and $n_0=3.6\times10^{21}$ m^{-3} resulting in a scattering parameter of $\alpha=0.20$. Method III illustrates the result of the weighted least mean squares fits if no coherent effects are taken into account and method IV shows the results of the analysis if coherent effects are taken into account. As can be seen method IV gives approximately ten times smaller relative differences between fit and simulation than method III. Although the error in n_e and T_e is on the order of α^2, the error in the determination of n_0 is larger. The error made in n_0 if no coherent effects are included, i.e., the difference between n_0 obtained from method IV and n_0 obtained from method III, where $n_{0,\mathrm{IV}}-n_{0,\mathrm{III}}$ can be expressed in $n_{e,\mathrm{IV}}$, the electron density obtained using method IV, and in the error in the electron density, $n_{e,\mathrm{IV}}-n_{e,\mathrm{III}}$:

$$n_{0,\mathrm{IV}}-n_{0,\mathrm{III}} = (\mathcal{N}+\beta)(n_{e,\mathrm{III}}-n_{e,\mathrm{IV}}) + \alpha^2\mathcal{N}n_{e,\mathrm{IV}}. \quad (6)$$

Here $\mathcal{N}$ is the ratio between the differential Thomson and differential Rayleigh cross section. $\mathcal{N}$ is equal to 143.[16] As can be seen from Eq. (6) the error becomes larger for a setup using a Ruby laser[9,11,12,33] since the ratio of the cross sections is larger in that case (the Rayleigh cross section is inversely proportional to λ^4). In Fig. 6 the error $n_{0,\mathrm{IV}}-n_{0,\mathrm{III}}$ is depicted versus $n_{e,\mathrm{IV}}$ for different $n_{e,\mathrm{IV}}-n_{e,\mathrm{III}}$ for $\alpha=0.20$. It appears that the correction in n_0 can be appreciable in the parameter range of the expanding cas-

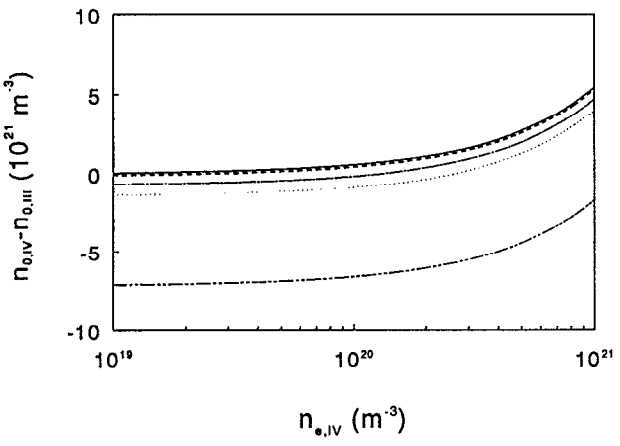

FIG. 6. The error $n_{0,IV} - n_{0,III}$ as a function of $n_{e,IV}$ for $\alpha = 0.20$ for different $n_{e,IV} - n_{e,III}$ equal to: (—)0, (----)10^{18} m^{-3}, (—·—)5×10^{18} m^{-3}, (·····)10^{19} m^{-3}, (—··—)5×10^{19} m^{-3}.

caded arc plasma even when $n_{e,IV} = n_{e,III}$, i.e., when the electron densities obtained by the two methods are the same.

To conclude this section the accuracy in n_e, n_0, and T_e is discussed. The following factors are of influence: (1) shot noise in signal (Poisson statistics); (2) laser: (a) energy stability (pulse to pulse), (b) pulse energy distribution both in time and spatial sense, (c) beam pointing stability; (3) detector: (a) light amplifier—(i) noise in quantum efficiency photocathode, (ii) noise in amplification factor, (iii) variation in time structure gate pulse (this has consequences for the amplification of the signal), (b) OMA—(i) noise in dark current, (ii) noise in AD conversion, (iii) reset noise photodiode element; (4) calibration: (a) relative—accuracy in the dispersion, (b) absolutely—determination of the pressure of the gas sample; (5) reproducibility in the conditions of the plasma. The main important noise factors are the shot noise and the combined noise of the detector and laser. To indicate the influence of the laser and detector in the noise contribution a typical Rayleigh calibration is discussed. The measurement consisted of ten measurements of 1200 shots at a 200-Pa argon sample. The mean value of the amount of counts was $N_{\text{Rayleigh}} = 67\,000 \pm 500$ AD counts. Here the uncertainty corresponds to the measured standard deviation. On the basis of Poisson statistics [see Eq. (1)] $\Delta N^{\text{Poisson}}_{\text{Rayleigh}} \simeq (67\,000\times3.4)^{1/2}/3.4 \simeq 140$ ADC counts are expected. It can be seen that the measured standard deviation is a factor of four higher indicating that other noise sources are of comparable size in this case. This other noise source is of course the combined laser and detector effect. For instance the pulse to pulse stability alone is already 2%. In case a large amount of shots is taken this pulse to pulse stability is averaged and reduces to approximately a random error of 1%. The same holds for the stability of the gain of the detector. For this purpose a so-called excess noise factor can be introduced. This factor, unknown for the used light amplifier, is estimated to be approximately 1.5–2, which means that the Poisson noise is amplified by the same factor. So the random error in n_e is mainly determined by the

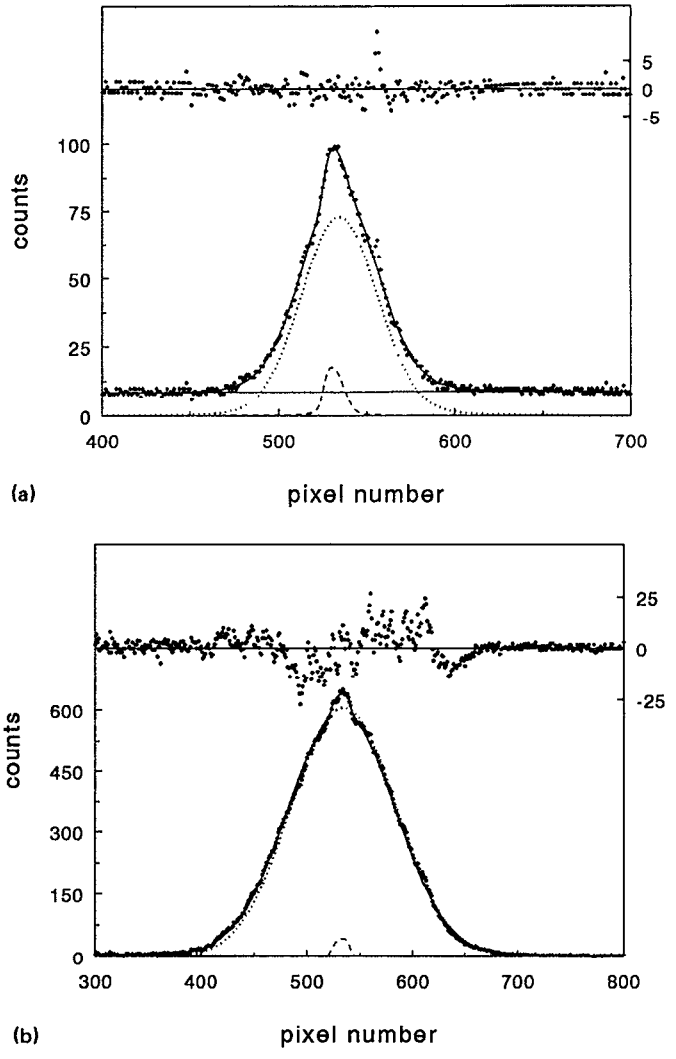

FIG. 7. Two measured Thomson–Rayleigh profiles, their weighted least mean squares fit and the corresponding residue. (a) $T_e = 5400 \pm 100$ K, $n_e = (4.65 \pm 0.09)\times10^{19}$ m^{-3}, and $n_0 = (7.2 \pm 0.7)\times10^{21}$ m^{-3}. (b) $T_e = 23100 \pm 500$ K, $n_e = (3.72 \pm 0.04)\times10^{19}$ m^{-3}, and $n_0 = (8.6 \pm 0.9)\times10^{19}$ m^{-3}, (·····) Thomson and (----) Rayleigh component.

instrumental noise and the Poisson noise. Typical values of the accuracies in n_e are, respectively, 1%–4%. For the error in n_e this means that the reproducibility in the plasma conditions, estimated to be within 1%, can play an important role. There is also some systematic error in n_e due to the calibration both relatively and absolutely ($\lesssim 2\%$). The errors in T_e are mainly determined by the analyzing procedure and the accuracy in the width in pixels. Furthermore, the error in T_e increases rapidly as the electron density goes down. For electron densities in the range 10^{18} m^{-3} the error in T_e is approximately 300–500 K. Typical errors in T_e are 2%–6%. Systematic errors in T_e are due to the determination of the dispersion on the Rowland circle ($\pm 1\%$) and the relative calibration ($\lesssim 2\%$). The accuracy in n_0 is mainly determined by the accuracy in the vessel straylight and the amplitude of the Rayleigh signal. Usually the relative error in n_0 is on the order of 10%–50%. Another important aspect is the inclusion of the coherent effects in the Thomson profile. If these effects are

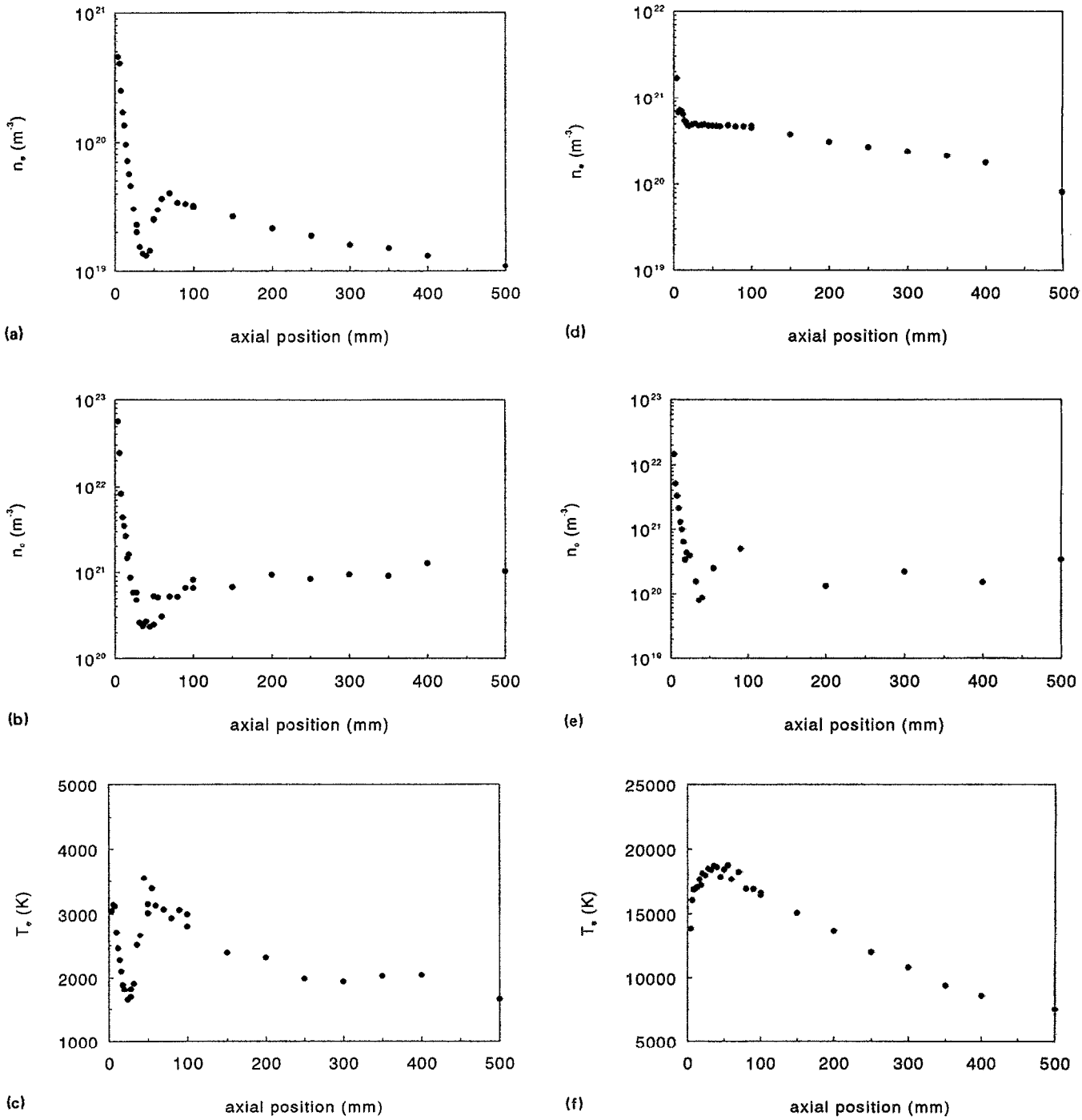

FIG. 8. The measured n_e, n_0 and T_e as a function of the axial position for the plasma conditions: (a)–(c) current cascaded arc $I_{cas} = 45$ A, argon gas flow $Q = 58$ scc/s, background pressure $p_{back} = 40$ Pa, no magnetic field and no current in jet section, (d)–(f) identical to (a)–(c) except magnetic field $B_z = 0.2$ T and current in jet section $I_{jet} = 45$ A.

not included it causes systematic errors in the determination of n_e, n_0, and T_e depending on α.

IV. RESULTS

In Fig. 7 two measured Thomson–Rayleigh profiles are given for two plasma conditions as indicated in the figure caption. Also the weighted least mean square fits are shown and the five times magnified residue. For Fig. 7(a) the scattering parameter was $\alpha \simeq 0.11$ and for Fig. 7(b) $\alpha \simeq 0.16$. Comparing Figs. 7(a) and 7(b) the large difference in temperature is immediately seen. This is because in Fig. 7(b) a magnetic field is applied and current is driven in the expansion section. The fact that in Fig. 7(b) the Rayleigh contribution is diminished is due to the ionization of the plasma which takes place in the expansion zone.

In Fig. 8 the corresponding axial dependences of the neutral particle and electron density and the electron temperature are shown. Figures 8(a)–8(c) clearly indicate a

free expanding plasma jet followed by a stationary shock front after which the plasma expands further subsonically. One point has to be mentioned here, i.e., the fact that the jump in the electron temperature occurs earlier than the jump in the densities. This has two reasons. The first one is because current generation occurs by the strong pressure gradient in the first section of the expansion.[12,34] A second reason is the large heat conduction of the electrons which causes a leakage from the higher temperature region in the shock.[2,35,36] A subsequent paper will be devoted to this subject. Figures 8(d)–8(f) show the influence of current and a magnetic field in the jet zone. The increase in density in the expansion zone is due to confinement of the plasma jet by the applied magnetic field. Ohmic dissipation increases the temperature and the plasma becomes ionizing.

ACKNOWLEDGMENTS

The authors wish to thank M. J. F. van de Sande and A. B. M. Hüsken for their skillful technical assistance, and Zhou Qing for his help during the construction of the setup.

[1] G. Poissant and M. Dudeck, J. Appl. Phys. **58**, 1772 (1985).
[2] R. B. Fraser, F. Robben, and L. Talbot, Phys. Fluids **14**, 2317 (1971).
[3] M. J. de Graaf, R. P. Dahiya, J. L. Jeauberteau, F. J. de Hoog, M. J. F. van de Sande, and D. C. Schram, Coll. Phys. **18**, C5-387 (1990).
[4] R. C. Jenkins, AIAA J. **9**, 1383 (1971).
[5] G. M. W. Kroesen, D. C. Schram, A. T. M. Wilbers, and G. J. Meeusen, Contr. Plasma. Phys. **31**, 27 (1991).
[6] C. Park, J. Plasma. Phys. **9**, 217 (1979).
[7] F. Siemsen, Bericht der Kernforschungsanlage Jülich Nr. 926 (1973).
[8] R. M. Patrick, Phys. Fluids **8**, 1985 (1965).
[9] O. Igra, Prog. Aerospace Sci. **16**, 299 (1975).
[10] R. Hidaka, T. Ooki, K. Takeda, K. Kondo, H. Kanada, K. Uchino, Y. Matsuda, K. Muraoka, and M. Akazaki, Jpn. J. Appl. Phys. **26**, L1724 (1987).
[11] A. V. Antsupov, Sov. Phys. Tech. Phys. **19**, 234 (1974).
[12] D. H. McNeil, Phys. Fluids **18**, 74 (1975).
[13] D. E. Evans and J. Katzenstein, Rep. Prog. Phys. **32**, 207 (1969).
[14] A. J. D. Farmer and G. N. Haddad, J. Phys. D **21**, 426 (1988).
[15] Z. Wang and R. Kearney, J. Quant. Spectrosc. Radiat. Transfer **44**, 339 (1990).
[16] P. Jauernik, H. Kempkens, and J. Uhlenbusch, Plasma Phys. Contr. Fusion **29**, 1615 (1987).
[17] M. Huang and G. Hieftje, Spectrochim. Acta **44** B, 739 (1989).
[18] H. Röhr, K.-H. Steuer, G. Schramm, K. Hirsch, and H. Salzmann, Nucl. Fusion **22**, 1099 (1982).
[19] A. Goehlich, V. Schulz-von der Gathen, and H. F. Döbele, Plasma Phys. Contr. Fusion **33**, 29 (1991).
[20] H. Maecker, Z. Naturforsch. **11** A, 457 (1956).
[21] J. L. Delcroix and A. R. Trinidade, Adv. Electron. Electron. Phys. **35**, 87 (1974).
[22] G. M. W. Kroesen, D. C. Schram, and M. J. F. van de Sande, Plasma Chem. Plasma Proc. **10**, 49 (1990).
[23] J. J. Beulens, G. M. W. Kroesen, D. C. Schramm, C. J. Timmermans, P. C. N. Crouzen, H. Vasmel, H. J. A. Schuurmans, C. B. Beijer, and J. Werner, J. Appl. Polymer Sci.: Appl. Polymer Symp. **46**, 527 (1990).
[24] G. J. Meeusen, Z. Qing, A. T. M. Wilbers, and D. C. Schram, invited lecture Intern. Conf. Thin Film Phys. and Appl. 1991 Shanghai, China.
[25] Jobin Yvon, Manual Concave gratings (1975).
[26] K. A. Marshall and G. M. Hieftje, Spectrochimica Acta **43** B, 851 (1988).
[27] M. C. M. van de Sanden, internal report (unpublished).
[28] S. E. Segre, Plasma Phys. **20**, 287 (1978).
[29] M. Huang and G. M. Hieftje, Spectrochimica Acta **44** B, 291 (1989).
[30] M. Huang and G. M. Hieftje, Spectrochimica Acta **45** B, 511 (1990).
[31] J. Sheffield, *Plasma Scattering of Electromagnetic Radiation* (Academic, New York, 1975).
[32] W. H. Press, B. P. Flannery, S. A. Teukolsky, and W. T. Vetterling, *Numerical Recipes in Pascal* (Cambridge University, Cambridge, 1989).
[33] B. van der Sijde, S. Adema, J. de Haas, C. J. M. Denissen, and M. J. F. van der Sande, Contr. Plasma. Phys. **22**, 357 (1982).
[34] G. M. Janssen, Internal report VDF/NT 91-13, University of Technology, Eindhoven, The Netherlands (1991).
[35] M. S. Grewal and L. Talbot, J. Fluid Mech. **16**, 573 (1963).
[36] R. H. Kirchhoff and L. Talbot, AIAA J. **9**, 1098 (1971).